Journal of
Materials Chemistry A

Materials for energy and sustainability

Accepted Manuscript

This article can be cited before page numbers have been issued, to do this please use: T. Liu, Q. Zhou, Y. Liu, Y. Zhang, R. Wang and Z. Chen, *J. Mater. Chem. A*, 2026, DOI: 10.1039/D6TA01093H.

ROYAL SOCIETY OF CHEMISTRY

rsc.li/materials-a

View Article Online
DOI: 10.1039/D6TA01093H

ARTICLE

Rational Design of RuO_2/0.5CeO_2 Heterostructure as an Efficient and Stable Electrocatalyst for Acidic Water Splitting

Received 00th January 20xx,
Accepted 00th January 20xx

DOI: 10.1039/x0xx00000x

Tenghao Liu[abc], Quan Zhou*[d], Liu Yang[d], Yining Zhang*[e], Rongyue Wang*[abc] and Zhongwei Chen*[d]

The large-scale commercialization of low-cost Ru-based catalysts in proton exchange membrane water electrolyzers (PEMWEs) is fundamentally hindered by structural degradation through lattice oxygen oxidation (LOM) pathways during acidic oxygen evolution reaction (OER). To address this challenge, we present an interfacial engineering strategy for the construction of ruthenium-cerium oxide heterostructure (RuO_2/xCeO_2) via a facile impregnation-pyrolysis method. Morphological and electronic structure characterizations confirm the formation of heterojunction interfaces between RuO_2 and CeO_2. The developed RuO_2/0.5CeO_2 catalyst achieves an overpotential of 214 mV and maintains negligible activity loss over 550 h at 10 mA cm^{-2}. Furthermore, the membrane electrode assembly (MEA) employing RuO_2/0.5CeO_2 as the anode delivers 1.59 V at 1 A cm^{-2} with over 300 h durability at 500 mA cm^{-2}, showcasing its practicality for PEMWE. Electronic structure analysis confirms the interfacial charge transfer lower the oxidation state of Ru species and diminish lattice oxygen content. Catalytic mechanism investigations and density functional theory (DFT) calculations reveal that the formation of heterointerface induces a transition in RuO_2 from a hybrid mechanism to an adsorbate evolution mechanism (AEM)-dominated OER pathway, lowering the energy barrier of the rate-determining step while suppressing lattice oxygen participation, synergistically enhancing activity and durability. This work proposes an effective strategy for designing highly active and durable ruthenium-based catalysts.

1. Introduction

Proton exchange membrane water electrolysis (PEMWE) has gathered significant attention due to its advantages, including rapid response time, high energy density, and high hydrogen purity.[1–3] However, PEMWE requires higher overpotential and consumes more energy to overcome the energy barrier, as the anodic oxygen evolution reaction (OER) involves a four-electron transfer process[4–6] , necessitating advanced efficient catalysts. To date, iridium (Ir)-based and ruthenium (Ru)-based catalysts are considered the most effective candidates in acidic environments. Nevertheless, the scarcity of Ir metal resource and relatively low OER activity are major factors limiting their widespread application.[7–9] Ru-based catalysts, particularly ruthenium dioxide (RuO_2), are widely regarded as promising alternatives to Ir-based catalysts due to their lower cost and higher OER activity.[10,11] Despite its advantages, at high OER potential, the Ru in RuO_2 is prone to over-oxidation, forming soluble RuO_4 via high-valent oxygen states, which leads to Ru dissolution and a rapid decay in catalyst activity and stability.[12,13] Therefore, enhancing the stability of RuO_2-based catalysts without compromising their activity is crucial for advancing the practical application of PEMWE.

To address this challenge, researchers have employed a range of strategies, including elemental-doping,[14–16] defect engineering,[17–19] construction of heterostructures,[20–22] and support materials interactions,[23,24] etc. Among these, the construction of heterogeneous interface structures stands out due to its unique structural features, such as synergistic effects,[25,26] strain effects,[27,28] and electronic interactions.[13,29] These features, which facilitate the modification of the electronic properties of the original catalyst, optimize the interface charge distribution and promote the kinetics of oxygen evolution reaction.[30] For example, Deng et al.[31] reported that constructing a CoO_x/RuO_x-CC heterointerface utilizes strong catalyst-support interactions to modify the electronic configuration of Ru-O bonds, achieving high acidic OER activity with an overpotential of 180 mV at 10 mA cm^{-2} and maintaining a stable current density of 100 mA cm^{-2} for 100 h. Wu et al.[32] engineered N-doped carbon-coated porous Ru/RuO_2 heterojunction hollow spheres to modulate the electronic configuration of Ru active sites to optimize the adsorption of intermediates, demonstrating exceptional OER performance with a low overpotential of 211 mV at 10 mA cm^{-2} and stability exceeding 120 h. However, pioneering heterostructure catalysts demand intrinsically carbon-free architectures to withstand harsh anodic conditions, alongside precisely

[a] National Engineering Research Center of Nonferrous Metals Materials and Products for New Energy, China GRINM Group Co., Ltd., Beijing 100088, China. E-mail: wangrongyue@grinm.com
[b] GRINM (Guangdong) Institute for Advanced Materials and Technology, Foshan, 528000, China.
[c] General Research Institute for Nonferrous Metals, Beijing 100088, China.
[d] State Key Laboratory of Catalysis, Power Battery & Systems Research Center, Dalian Institute of Chemical Physics, Chinese Academy of Sciences, Dalian 110623, China. E-mail: zhouquan2010@dicp.ac.cn; zwchen@dicp.ac.cn
[e] High-Performance Lithium-Ion Battery Research and Development Center, Yulin Innovation Institute of Clean Energy, Yulin, 719004, China. E-mail: zhangyn@dnlyl.ac.cn

View Article Online
DOI: 10.1039/D6TA01087H

adjustable heterocomponent ratios. In recent years, CeO_2 has been widely employed as an electronic promoter in host electrocatalysts to regulate oxygen vacancy dynamics, leveraging its reversible Ce^{3+}/Ce^{4+} redox couple.[33–36] Motivated by recent advances in CeO_2-based electrocatalysts, the rational design of RuO_2/CeO_2 heterostructures has emerged as a promising strategy to suppress Ru overoxidation while enhancing acidic OER activity. However, most reported Ru-Ce systems still rely on carbon-based supports that are susceptible to anodic corrosion, which limits their long-term applicability under PEMWE conditions. In addition, precise control over the Ru/Ce ratio and systematic optimization of heterointerface composition remain insufficiently explored.

Herein, we developed a facile impregnation-pyrolysis approach to synthesize RuO_2 and CeO_2 nanoparticle heterostructure catalysts, featuring abundant heterogeneous interfaces, where morphological characterization verified the formation of RuO_2-CeO_2 heterostructures. When utilized as an acidic OER catalyst, $RuO_2/0.5CeO_2$ exhibits a low overpotential of 214 mV at 10 mA cm^{-2} and sustains negligible activity degradation over 550 h at 10 mA cm^{-2}, demonstrating enhanced performance compared to commercial RuO_2. Furthermore, the membrane electrode assembly (MEA) integrated with $RuO_2/0.5CeO_2$ as anode delivers an outstanding performance of 1.59 V at 1 A cm^{-2} with long-term stability of over 300 h at 500 mA cm^{-2}. Mechanistic studies and theoretical calculations demonstrate that $RuO_2/0.5CeO_2$ heterointerface induces a transition from the original hybrid mechanism to an adsorbate evolution mechanism (AEM)-dominated OER pathway. This shift suppresses lattice oxygen oxidation while accelerating *OOH intermediate formation, synergistically enhancing both catalytic activity and operational durability.

2. Materials and methods

2.1. Chemicals and materials

$RuCl_3 \cdot nH_2O$ (Kunming Boren Precious Metals Co.Ltd), $CeCl_3 \cdot 7H_2O$ (Aladdin, 99.99%), carbon black (Black Pearls 2000, abbreviated as BP2000), cyanamide (95%, Macklin), commercial Pt/C (60%Pt, Johnson Matthey Hispec9100), and commercial RuO_2 (Aladdin, 99.99%).

2.2. Synthesis of catalysts

0.128 g of $RuCl_3 \cdot nH_2O$, 0.087 g of $CeCl_3 \cdot 7H_2O$ and 0.295 g of cyanamide were dissolved in 20 ml of deionized water and ultrasonicated for 10 minutes to form a uniform solution. Subsequently, 0.317 g of BP2000 carbon was added to the solution and stirred for 30 minutes to form a homogeneous mixture. Finally, the mixture was vacuum-dried at 80 °C to obtain precursor powder. The precursor powder was annealed at 650 °C for 2 h in a tube furnace under a 10 vol% H_2/N_2 atmosphere, yielding an intermediate compound designated as Ru-CeOCl/C. This intermediate was subsequently calcined at 450 °C for 5 h under ambient air atmosphere to obtain final product, namely $RuO_2/0.5CeO_2$.

For comparative analysis, samples were prepared by varying the mass of $CeCl_3 \cdot 7H_2O$ precursor while maintaining identical procedures for other synthesis steps. Specifically, samples prepared with 0.175 g and 0.038 g $CeCl_3 \cdot 7H_2O$ were denoted as RuO_2/CeO_2 and $RuO_2/0.25CeO_2$, respectively. Reference samples synthesized in the absence of $CeCl_3 \cdot 7H_2O$ and $RuCl_3 \cdot nH_2O$ were denoted as homemade RuO_2 and homemade CeO_2, respectively.

2.3. Characterization

Crystal Structure of catalysts was conducted by XRD. A Malvern Panalytical Empyrean S3 diffractometer equipped with a Cu Kα source generated diffraction profiles across a 2θ range of 10-90°. X-ray photoelectron spectroscopy (XPS) measurements were performed on a Thermofisher Escalab 250 Xi+ (Thermo Scientific), using Al Kα radiation as the excitation source. Transmission electron microscopy (TEM) was conducted with a JEM-2100 microscope. High-angle annular dark field scanning transmission electron microscopy (HAADF STEM) was carried out using a JEM-ARM200F microscope 200 KV. Scanning electron microscopy (SEM) was performed with a Sigma 560 field emission scanning electron microscope equipped with energy-dispersive X-ray spectroscopy (EDS) for elemental analysis. Inductively Coupled Plasma Optical Emission Spectroscopy (ICP-OES) analysis was carried out using a Thermofisher Escalab 250 Xi^+.

2.4. Electrochemical OER measurements

Electrochemical measurements were evaluated in 0.1 M $HClO_4$ electrolyte with a three-electrode setup on a CHI 760E workstation. Glassy carbon electrode (GCE) with a 5 mm diameter was used as working electrode. Ag/AgCl electrode with saturated KCl solution and graphite rod were used as reference electrode and counter electrode, respectively. The measured potential was converted to a reversible hydrogen electrode (RHE) using the following equation:

$$E_{RHE}=E_{Ag/AgCl}+0.059\times pH+0.197 \quad (1)$$

A homogeneous catalyst ink was prepared by ultrasonically dispersing 16 mg of catalyst for 30 min in a solvent mixture of 0.5 ml of ultrapure water, 0.48 ml of anhydrous ethanol, and 20 µl of Nafion solution (5wt% Nafion, Dupont D520). The catalyst thin film on the working electrode was fabricated by depositing homogenized catalyst ink onto a glassy carbon substrate, resulting in a catalyst loading of 0.36 mg_{Ru} cm^{-2}. The electrode was first activated through electrochemical cycling between 1.05 and 1.75 V vs. RHE at 100 mV s^{-1} for 30 cycles. Linear sweep voltammetry (LSV) measurements with iR compensation were conducted over a potential range of 1.05 to 1.65 V versus RHE at a scan rate of 10 mV s^{-1}. Electrochemical impedance spectroscopy (EIS) measurements were carried out with the frequency range from 10,000 Hz to 0.1 Hz with an amplitude of 5 mV. The Tafel slope is calculated according to following equation:

$$\eta=b\times\log j+a \quad (2)$$

View Article Online DOI: 10.1039/D6TA01057H

Where η is the overpotential, b is the Tafel slope, j is the current density, and a is a constant. The ECSA of the catalysts were quantified via the electrochemical double-layer capacitance (C_{dl}) according to the following equation:

$$ECSA=\frac{C_{dl}}{C_s}(3)$$

Where C_{dl} was via cyclic voltammetry at scan rates of 2-10 mV s^{-1} within a non-Faradaic potential range (0.87-0.97 V vs. RHE), as derived from the linear slope of capacitive current versus scan rate plots. C_s is the general surface specific capacitance (0.035 mF cm^{-2}). The turnover frequency (TOF) of catalysts was determined using following equation:

$$TOF(O_2h^{-1})=3600\times\frac{O_2\text{ turnovers per }A_{geo}}{\text{active sites per }A_{geo}}(4)$$

Where the calculation of O_2 turnovers per geometric area is according to following equation:

$$O_2\text{ turnovers per}A_{geo}=j_{geo}\times\frac{1Cs^{-1}}{1000mA}\times\frac{1mol}{96485.3C}\times\frac{1}{4}\times\frac{6.023\times10^{23}}{1molO_2}(5)$$

All Ru atoms in the catalyst are assumed to be active sites. SEM-EDS results were used to calculate the number of active sites per geometric area. Chronopotentiometry (CP) tests were conducted at 25 °C using titanium mesh electrodes coated with catalyst via spray deposition, with a controlled mass loading of 1.6 mg_{Ru} cm^{-2}.

2.5. In situ Attenuated Total Reflection Surface-Enhanced Infrared Absorption Spectroscopy (ATR-SEIRAS) experiments

in situ ATR-SEIRAS experiments were performed on a Nicolet iS50 FT-IR spectrometer equipped with a narrow band MCT-A detector and an in situ IR optical accessory (SPEC-I, Shanghai Yuanfang Tech.) Unpolarized infrared spectra were acquired at 8 cm^{-1} resolution. Nano scale gold thin films were chemically deposited on silicon substrates to amplify infrared signal sensitivity and conductivity. A homogeneous catalyst ink was prepared by ultrasonically dispersing 2 mg of catalyst for 30 min in a solvent mixture of 0.28 ml ultrapure water, 0.7 ml anhydrous ethanol, and 20 µl Nafion solution (5wt% Nafion, Dupont D520). 20 µl of the ink was uniformly coated onto the Au-modified surface, serving as the working electrode in a three-electrode electrochemical cell. Ag/AgCl electrode with saturated KCl solution and Pt mesh were used as reference electrode and counter electrode, respectively.

2.6. PEMWE testing

Membrane electrode assemblies (MEAs) were fabricated via the catalyst coated membrane (CCM) method, employing $RuO_2/0.5CeO_2$ as the anode catalyst and commercial Pt/C (60 wt% Pt, Johnson Matthey Hispec9100) as the cathode catalyst. The catalyst powder was dispersed in isopropanol, deionized water, and Nafion solution to prepare the ink. The resulting anode and cathode inks were uniformly deposited by spray coating onto opposing sides of a Nafion 115 proton exchange membrane (active area: 5 cm^2), achieving precise loadings of 1.0 mg_{Ru} cm^{-2} and 0.3 mg_{Pt} cm^{-2}, respectively. CCM, anode gas diffusion layer (platinum-coated titanium felt), and cathode gas diffusion layer (carbon paper) were hot-pressed to obtain a MEA. For comparison, a control MEA with commercial RuO_2 anode was similarly prepared. PEM electrolyzers were operated at 80 °C with distilled water as reactant. A chronopotentiometry test was performed at 500 mA cm^{-2} to evaluate the durability of $RuO_2/0.5CeO_2$.

2.7. DFT calculations

Density functional theory (DFT) calculations were carried out using the Vienna ab initio simulation package (VASP) to determine the system geometries and energies. The projector augmented wave (PAW) method was employed to model the interactions between ion cores and valence electrons. For the exchange-correlation functional, the Perdew-Burke-Ernzerhof (PBE) variant of the generalized gradient approximation (GGA) was utilized. The electronic wave functions were expanded in a plane-wave basis set, with a kinetic energy cutoff of 520 eV applied. Brillouin zone integration was performed using a Monkhorst-Pack k-point grid of dimensions 3 × 3 × 1. Structural optimization was conducted via a conjugate-gradient algorithm based on atomic forces, with convergence criteria set at 1.0 × 10^{-5} eV per atom for energy and 0.02 eV/Å for forces.

3. Results and Discussion

As depicted in Fig. 1a, the $RuO_2/0.5CeO_2$ electrocatalyst was fabricated through two-steps cyanamide-assisted impregnation-pyrolysis method. Briefly, aqueous mixture containing certain proportion of Ru salt, Ce salt, cyanamide (CN_2H_2), and carbon black were homogeneously mixed and then dried. Dry precursor was then annealed in a diluted H_2/N_2 atmosphere within a tube furnace, yielding carbon-supported Ru and CeOCl (denoted as Ru-CeOCl/C). Finally, the obtained Ru-CeOCl/C was calcined under air atmosphere to produce the $RuO_2/0.5CeO_2$ heterostructure electrocatalyst. (For a detailed description of the preparation process, see Experimental Section.) The experimental XRD pattern of $RuO_2/0.5CeO_2$ matches the standard reference cards for RuO_2 (PDF#43-1027) and CeO_2 (PDF#89-8436), confirming the coexistence of crystalline RuO_2 and CeO_2 phases (Fig. 1b). Notably, all RuO_2 diffraction peaks in the $RuO_2/0.5CeO_2$ undergo a positive shift, indicating lattice contraction within the RuO_2 phase due to heterostructure-induced strain, which is consistent with previously reported results of MnO_2/RuO_2.[37] Subsequently, a series of heterostructured catalysts were synthesized by adjusting the amount of Ce salt precursor. XRD patterns of both RuO_2/CeO_2 and $RuO_2/0.25CeO_2$ samples confirmed a positive shift in RuO_2 diffraction peaks (Fig. 1c). With decreasing adding amount of cerium precursor, the $RuO_2/0.25CeO_2$ sample displays coexisting crystalline phases of metallic Ru and RuO_2. Control experiments indicate that cyanamide is crucial for heterostructure construction. As shown in Fig. S1, without cyanamide, the final product shows RuO_2 diffraction peaks at the standard bulk positions, whereas the cyanamide-assisted route induces peak shifts characteristic of interfacial coupling, suggesting that cyanamide promotes intimate Ru-Ce precursor

View Article Online
DOI: 10.1039/D5TA01067H

mixing and facilitates RuO_2/CeO_2 heterostructure formation during annealing. Homemade RuO_2 and CeO_2 were synthesized for comparison, where the RuO_2 phase exhibits perfect consistency with the standard PDF card, further confirming that the RuO_2 peak shift in $RuO_2/xCeO_2$ samples resulted from lattice contraction induced by heterostructure formation.

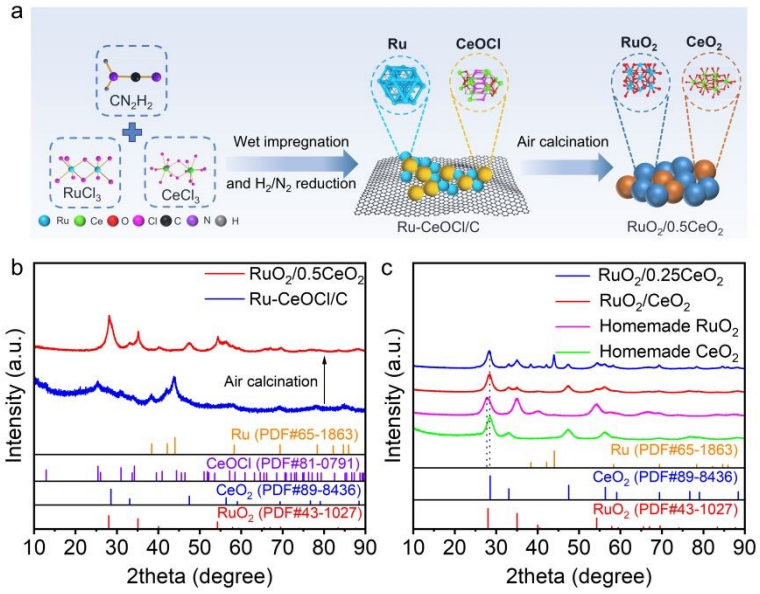

Fig. 1 (a) Schematic illustration of the synthesis of $RuO_2/0.5CeO_2$ catalyst. (b) XRD patterns of $RuO_2/0.5CeO_2$ and Ru-CeOCl/C. (c) XRD patterns of $RuO_2/0.25CeO_2$, RuO_2/CeO_2, homemade RuO_2, and homemade CeO_2.

The morphology and composition of heterostructured catalysts were characterized by scanning electron microscopy (SEM) and SEM-Energy Dispersive X-ray Spectroscopy (EDS) analysis (Fig. S2-S4). SEM-EDS analysis determines that the mass ratios of Ru and Ce in $RuO_2/0.5CeO_2$ are 42.48% and 32.3%, respectively, with an atomic ratio of approximately 1.9:1 (Fig. S3). The catalyst maintains minimal carbon content (3.2 wt%), matching commercial RuO_2 benchmarks, avoiding carbon-induced degradation pathways. The Ru-to-Ce ratios in other heterostructured catalysts, as determined by SEM-EDS and ICP-OES, are summarized in Table S1. Transmission electron microscopy (TEM) and aberration-corrected scanning transmission electron microscopy (ac-STEM) were used to characterize the morphology of the $RuO_2/0.5CeO_2$ catalyst. TEM image reveals abundant heterostructures featuring coherent interfaces formed between RuO_2 and CeO_2 nanoparticles (Fig. 2a, 2b). As shown in Fig. 2c, selected area electron diffraction (SAED) further identifies distinct diffraction rings of RuO_2 (211), (101), and (110), as well as the crystal facet of CeO_2 (111), (220) and (222).[38] HAADF-STEM image (Fig. 2d) and the enlarged atomic-resolution image (Fig. 2e) further reveal the intimate contact between adjacent nanodomains, where two representative regions (d1 and d2) were selected for FFT/IFFT analysis to identify the CeO_2 and RuO_2 phases at the heterointerface. As illustrated in Fig. 2f and 2g, fringes with a spacing of 0.31 nm corresponds to the (111) plane of cubic CeO_2, whereas fringes with a spacing of 0.247 nm belong to the (101) plane of RuO_2 (typically around 0.256 nm). The reduced lattice spacing of RuO_2 confirms heterostructure-induced contraction in RuO_2, consistent with XRD results. Furthermore, EDS elemental mapping of $RuO_2/0.5CeO_2$ further corroborates atomically intimate heterointerfaces with distinct boundaries between RuO_2 and CeO_2 nanoparticles (Fig. 2h).

View Article Online
DOI: 10.1039/D6TA01093H

ARTICLE

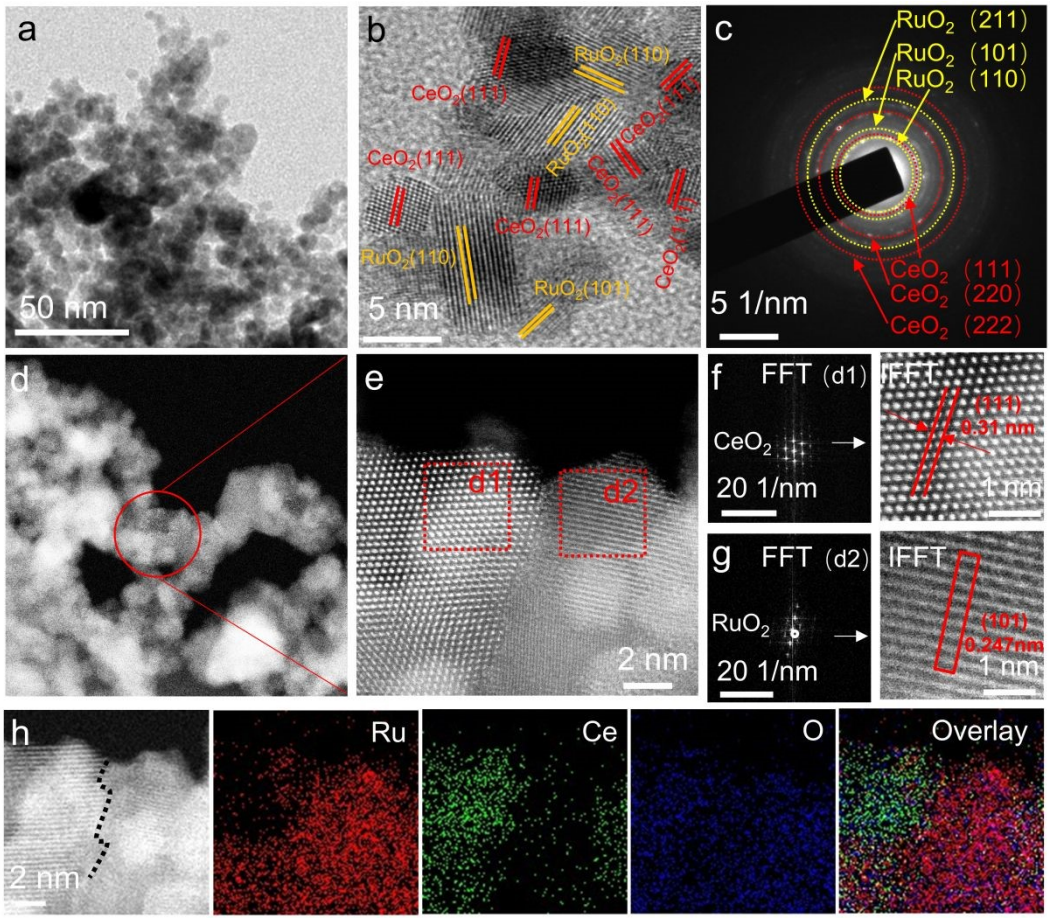

Fig. 2 (a) low-magnification TEM, (b) high-magnification TEM, and (c) corresponding SAED patterns of $RuO_2/0.5CeO_2$. (d) HADDF-STEM image and (e) enlarged atomic-resolution image of $RuO_2/0.5CeO_2$. FFT image and IFFT image of (f) CeO_2 and (g) RuO_2 taken from the corresponding regions in (e). (h) EDS elemental mapping images for $RuO_2/0.5CeO_2$.

To investigate the effects of heterogeneous interface on the electronic structure of $RuO_2/0.5CeO_2$ and the mechanistic roles in catalytic activity, we performed X-ray photoelectron spectroscopy (XPS) to characterize surface chemical states and interfacial electronic interactions. The survey-scan XPS analysis reveals Ru and O signatures in homemade RuO_2, whereas distinct Ru, Ce, and O spectral peaks emerge in $RuO_2/0.5CeO_2$, indicating the successful synthesis of $RuO_2/0.5CeO_2$ (Fig. 3a). As shown in Fig. 3b, the high-resolution Ru 3p spectrum of $RuO_2/0.5CeO_2$ exhibits two spin-orbit doublet peaks at 462.4 eV ($3p_{3/2}$) / 484.7 eV ($3p_{1/2}$) and 465.5 eV ($3p_{3/2}$) / 487.8 eV ($3p_{1/2}$), corresponding to Ru^{4+} and Ru^{3+} species respectively. Compared with pristine RuO_2, the Ru $3p_{3/2}$ spectra of $RuO_2/0.5CeO_2$ exhibits a 0.39 eV negative shift, accompanied by an increased Ru^{3+} fraction, indicating interfacial electronic redistribution and increased electron density at Ru sites in the heterostructure.[39] Meanwhile, the Ce 3d spectrum shows a positive shift (0.68 eV) together with a higher Ce^{4+} proportion relative to CeO_2, further supporting interfacial charge redistribution between CeO_2 and RuO_2 (Fig. 3c). This evidence aligns with electron transfer from CeO_2 to Ru atoms. which consequently reduces the average valence state of Ru species.[35] The O 1s spectra were deconvoluted into four peaks: lattice oxygen (O_L), hydroxyls (-OH), adsorbed H_2O, and C=O or C−O species (Fig. 3d).[40] Relative to pristine RuO_2, the lattice oxygen peak in $RuO_2/0.5CeO_2$ displays a 0.14 eV higher binding energy, indicating transfer of electrons from lattice oxygen to metal sites and result in reduced oxidation state of Ru species.[41] The lower valence state suppresses electron transfer from Ru/Ce atoms to oxygen, while altered local coordination environments may optimize reaction pathways.[42] The binding energy position and relative concentrations of O 1s for $RuO_2/0.5CeO_2$ and RuO_2 are summarized in Table S2. These findings confirm the successful construction of a Ru-based heterostructure catalyst with a reduced Ru oxidation state, where electron transfer from CeO_2 to RuO_2 modulates the electronic structure and suppresses

View Article Online
DOI: 10.1039/D6TA01097H

lattice oxygen participation, thereby potentially enhancing OER kinetics. The interfacial electron redistribution between CeO_2 and RuO_2 is expected to optimize the Ru–O electronic environment, rather than merely lowering the Ru valence. Such modulation can balance the adsorption/desorption of oxygenated intermediates on Ru sites and suppress excessive lattice-oxygen activation, thereby favoring faster and more stable OER kinetics.

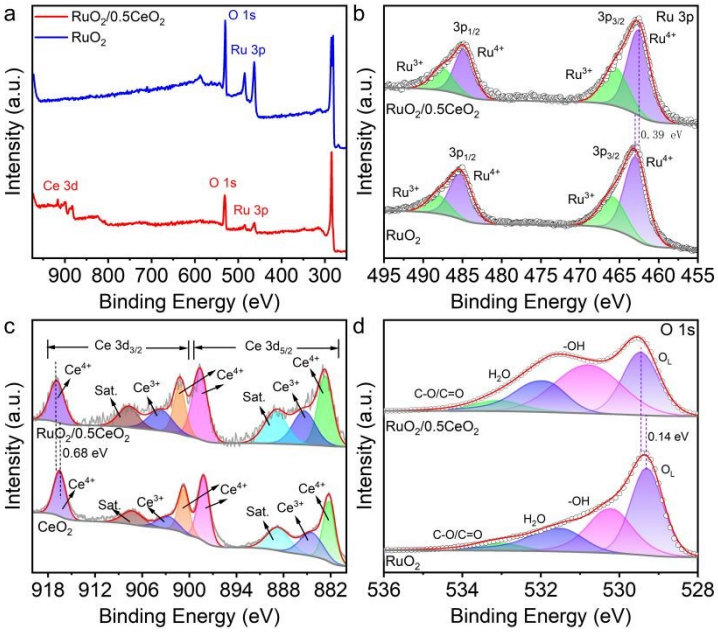

Fig. 3 (a) XPS survey spectrum of $RuO_2/0.5CeO_2$ and commercial RuO_2. High-resolution XPS spectra of (b) Ru 3p for $RuO_2/0.5CeO_2$ and commercial RuO_2, (c) Ce 3d for $RuO_2/0.5CeO_2$, and (d) O 1s for $RuO_2/0.5CeO_2$ and commercial RuO_2.

The OER performance of as-prepared catalysts in 0.1 M $HClO_4$ electrolyte were evaluated via a standard three-electrode system. The linear sweep voltammetry (LSV) curves reveal that $RuO_2/0.5CeO_2$ significantly outperforms RuO_2/CeO_2, $RuO_2/0.25CeO_2$, homemade RuO_2 and commercial RuO_2 in terms of current density (Fig. 4a and S5). Specifically, the overpotential of the $RuO_2/0.5CeO_2$ requires only 214 mV overpotential at 10 mA cm^{-2}, substantially lower than homemade RuO_2 (251 mV), $RuO_2/0.25CeO_2$ (259 mV), RuO_2/CeO_2 (308 mV), and commercial RuO_2 (304 mV), respectively, while homemade CeO_2 negligible OER activity (Fig. 4b). Furthermore, the $RuO_2/0.5CeO_2$ requires only 266 mV overpotential at 100 mA cm^{-2}, surpassing than those of other catalysts. The Tafel slope of 48.9 mV dec^{-1} for $RuO_2/0.5CeO_2$ further evidences faster OER kinetics compared to $RuO_2/0.25CeO_2$ (73.5 mV dec^{-1}), RuO_2/CeO_2 (142.8 mV dec^{-1}), and commercial RuO_2 (141.1 mV dec^{-1}) (Fig. 4c). Electrochemical impedance spectroscopy (EIS) reveals that $RuO_2/0.5CeO_2$ exhibits the lowest charge transfer resistance (R_{ct}) at 1.5 V vs. RHE among all catalysts, demonstrating superior OER kinetics (Fig. S6). Operando EIS measurements were employed to probe interfacial charge transfer dynamics in $RuO_2/0.5CeO_2$. Fig. 4d and 4e present Bode phase plots comparing the catalyst with commercial RuO_2. At high frequencies (10^1-10^3 Hz), the catalyst exhibits reduced charge-transfer resistance compared to commercial RuO_2, indicating accelerated electron mobility through Ru-O-Ce bonding networks at the surface-oxidation interface. Concurrently, at lower frequencies (10^{-1}-10^1 Hz), beyond an applied potential of 1.35 V, become smaller than that of commercial RuO_2, which could be attributed to the faster kinetics in adsorbed intermediates during OER in $RuO_2/0.5CeO_2$.[40,43] The electrochemical active surface area (ECSA) was evaluated via cyclic voltammetry at scan rates of 2-10 mV s^{-1} within a non-Faradaic potential range (Fig. S7). The electric double-layer capacitance (C_{dl}) was derived from the linear slope of capacitive current versus scan rate plots. As shown in Fig. 4f, $RuO_2/0.5CeO_2$ exhibits a highest C_{dl} of 37.3 mF cm^{-2}, 1.6-fold and 3.8-fold higher than $RuO_2/0.25CeO_2$ (23.6 mF cm^{-2}) and RuO_2/CeO_2 (9.8 mF cm^{-2}), confirming heterostructure-induced exposure of active sites that enhance catalytic kinetics. To compare the intrinsic activities of these catalysts, the ECSA-normalized current density was calculated, confirming the highest intrinsic activity of $RuO_2/0.5CeO_2$ compared with other catalysts (Fig. S8). The superior intrinsic activity of $RuO_2/0.5CeO_2$ is attributed to the RuO_2-CeO_2 heterointerface, which combines interfacial strain, charge redistribution, and surface hydroxyl enrichment to optimize the reaction energetics of OER intermediates, rather than relying solely on Ru valence reduction. Turnover frequency (TOF) values were derived from the oxygen evolution rate scaled to the total Ru ions (Fig. 4g). At 1.5 V, $RuO_2/0.5CeO_2$ yields a TOF of 942 h^{-1}, surpassing that of RuO_2/CeO_2 (58 h^{-1}), $RuO_2/0.25CeO_2$ (187 h^{-1}), and commercial RuO_2 (73 h^{-1}). As evidenced by the chronopotentiometry (CP) test at 10 mA cm^{-2} in Fig. 4h, $RuO_2/0.5CeO_2$ operates stably for over 550 h at 10 mA cm^{-2} with only 15 mV increase in potential, surpassing commercial RuO_2 (deactivation within 3 h) and outperforming most reported Ru-based electrocatalysts (Table S3). Post-stability ICP analysis of electrolytes was conducted to quantify metal dissolution. Additional post-stability TEM and XPS analyses reveal that,

View Article Online
DOI: 10.1039/D5TA01997H

despite partial Ce dissolution, the RuO_2 lattice and Ru chemical state are largely preserved after prolonged OER operation, indicating that Ce leaching mainly induces surface reconstruction rather than structural collapse of the heterostructure (Fig. S9).

As summarized in Table S4, the Ru dissolution rate of $RuO_2/0.5CeO_2$ is 0.115%, which is markedly lower than that of commercial RuO_2 (0.45%). Notably, the Ce dissolution rate in $RuO_2/0.5CeO_2$ is 16.4%, which could be ascribed to the sacrificing oxidation of CeO_2, thereby preserving RuO_2 active sites.

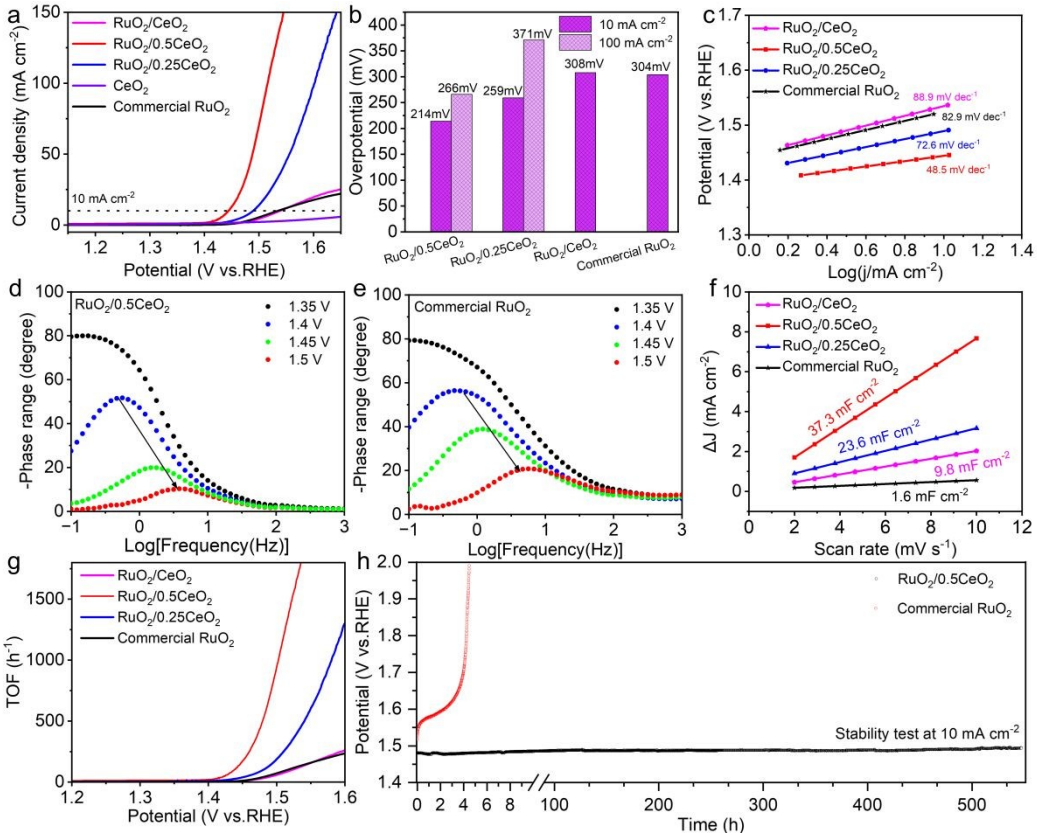

Fig. 4 (a) LSV polarization curves of RuO_2/CeO_2, $RuO_2/0.5CeO_2$, $RuO_2/0.25CeO_2$, commercial RuO_2, and homemade CeO_2 with iR compensation. (b) Overpotential comparisons at current densities of 10 and 100 mA cm^{-2}. (c) Tafel slopes derived from (a). Bode phase plots of (d) $RuO_2/0.5CeO_2$ and (e) commercial RuO_2 at different potentials. (f) C_{dl} plots derived from CV curves. (g) TOF of RuO_2/CeO_2, $RuO_2/0.5CeO_2$, $RuO_2/0.25CeO_2$, commercial RuO_2. (h) Chronopotentiometry test of $RuO_2/0.5CeO_2$ and commercial RuO_2 at 10 mA cm^{-2}.

Inspired by the outstanding OER performance and durability of the $RuO_2/0.5CeO_2$ catalyst, we further evaluated its practical applicability in a PEMWE device. The PEMWE configuration is illustrated in Fig. 5a. The anode catalyst was $RuO_2/0.5CeO_2$ with a Ru loading of 1 mg cm^{-2}, while the cathode catalyst was commercial Pt/C (60 wt% Pt, Johnson Matthey Hispec9100) with a Pt loading of 0.3 mg cm^{-2}. A Nafion N115 was served as the proton exchange membrane. For comparison, a control device was fabricated using commercial RuO_2 as the anode with a Ru loading of 1 mg cm^{-2}, while maintaining identical experimental conditions. As depicted in Fig. 5b, the current-voltage characteristic (I-V) curve (without iR correction) demonstrates that, $RuO_2/0.5CeO_2$ catalyst achieves a current density of 1 A cm^{-2} at 80 °C with an applied voltage of 1.59 V, whereas commercial RuO_2 requires 1.64 V under identical conditions. As illustrated in Fig. 5b, the I-V curves (without iR correction) demonstrate that, $RuO_2/0.5CeO_2$ only requires a cell voltage of 1.59 V and 1.72 V to reach a current density of 1 A cm^{-2} and 2 A cm^{-2}, surpassing commercial RuO_2 (1.64 V for 1 A cm^{-2} and 1.79 V for 2 A cm^{-2}). Furthermore, the $RuO_2/0.5CeO_2$ can operate over 300 h at 500 mA cm^{-2} with a performance degradation rate of only 0.07 mV h^{-1} (Fig. 5c), which outperforms most reported Ru-based electrocatalysts (Table S3). In addition, a comparison with representative previously reported Ru-Ce based catalysts is provided in Table S5. Relative to these systems, the present catalyst distinguishes itself by combining a carbon-free architecture, tunable Ru/Ce composition, and extended MEA validation, while maintaining competitive activity and durability. These features highlight the practical potential of the RuO_2-CeO_2 heterostructure for PEMWE operation under harsh acidic conditions.

View Article Online
DOI: 10.1039/D6TA01093H

ARTICLE

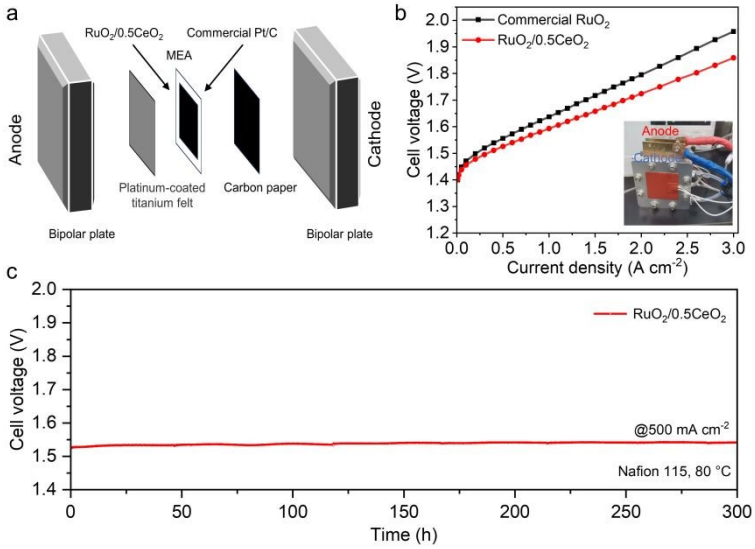

Fig. 5 (a) Schematic of the PEMWE device. (b) I-V curves of PEMWE electrolyzers using $RuO_2/0.5CeO_2$ or commercial RuO_2 as anodic catalyst and commercial Pt/C as cathodic catalyst in pure water at 80 °C without iR compensation. Inset in (b): photograph of the PEMWE device. (c) Chronopotentiometry testing of $RuO_2/0.5CeO_2$ catalyst at 500 mA cm^{-2} in the PEMWE electrolyzer using commercial Pt/C as cathodic catalyst in pure water at 80 °C.

pH-dependent experiments probing the OER mechanism reveal negligible dependence of catalytic activity on electrolyte pH (Fig. S9). At 2 mA cm^{-2}, overpotentials remained nearly identical across pH range from 0.3 to 1.0, with consistent behaviour extending to 5 mA cm^{-2} and 10 mA cm^{-2} (Fig. 6a). These observations collectively suggest that the reaction pathway is following the AEM mechanism, characterized by four coupled proton-electron transfers. In situ ATR-SEIRAS were further performed to gain deeper mechanistic insights into the acidic OER on $RuO_2/0.5CeO_2$ (Fig. 6b). The FTIR spectrum of $RuO_2/0.5CeO_2$ exhibits an O-H stretching mode of *OH at 3220 cm^{-1}, along with a prominent peak at 1041 cm^{-1} assigned to O-O stretching of *OOH intermediates. Given that *OOH represents a signature intermediate of the AEM mechanism, this observation indicates AEM dominance in the OER process (Fig. 6c). Critically, the absence of a *OO characteristic peak at approximately 1120-1130 cm^{-1} rules out the involvement of the LOM mechanism. [41,44] In contrast, while pristine RuO_2 is well-documented to exhibit a hybrid AEM/LOM mechanism in acidic OER.[41,45,46] The construction of $RuO_2/0.5CeO_2$ significantly suppresses the LOM pathway by stabilizing lattice oxygen. This electronic modulation mitigates Ru over-oxidation, ensuring the AEM pathway becomes highly dominant, thereby enhancing both catalytic activity and long-term stability. To elucidate the origin of catalytic activity in $RuO_2/0.5CeO_2$, DFT calculations were performed using a heterojunction model comprising RuO_2 (110) and CeO_2 (111) facets with a Ru:Ce atomic ratio of 2:1 (Fig. 6d and S10-S12). The RuO_2 (110) and CeO_2 (111) interfaces aligned well, forming extended coordinatively bridge row via Ru−O−Ce bonds. Both $RuO_2/0.5CeO_2$ and RuO_2 followed four-proton-coupled electron transfer steps of AEM, as shown in Fig. 6e and S10. The OER rate-determining step (RDS) for both $RuO_2/0.5CeO_2$ and RuO_2 is the transformation of *O to *OOH (Fig. 6f). Specifically, at the theoretical potential (U = 1.23 V), $RuO_2/0.5CeO_2$ exhibits a free energy barrier of 0.665 eV, which is 0.217 eV lower than that of pristine RuO_2 (0.882 eV). The lowered barrier promotes *OOH formation efficiency, demonstrating that heterostructure engineering in $RuO_2/0.5CeO_2$ is an effective strategy for boosting OER kinetics.

View Article Online
DOI: 10.1039/D6TA01093H

ARTICLE

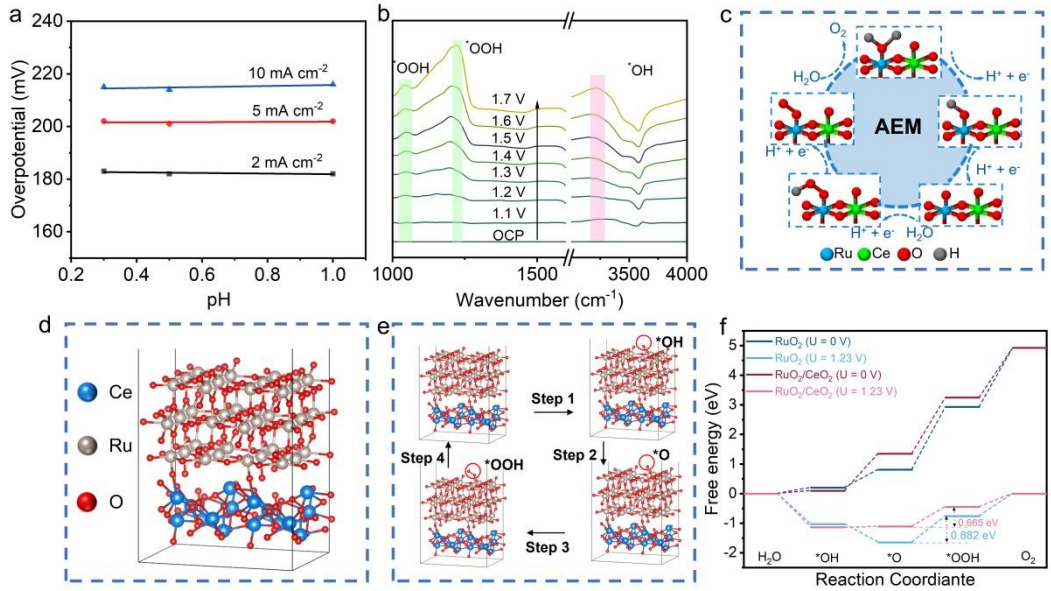

Fig. 6 (a) Overpotential of $RuO_2/0.5CeO_2$ at 2 mA cm^{-2}, 5 mA cm^{-2}, and 10 mA cm^{-2}, respectively, in electrolytes with different pH. (b) In situ ATR-SEIRAS spectra at various applied potentials for $RuO_2/0.5CeO_2$. (c) The AEM path diagram. (d) Crystal structure model of $RuO_2/0.5CeO_2$. (e) Four-step AEM of OER for $RuO_2/0.5CeO_2$. (f) Free energy diagrams of $RuO_2/0.5CeO_2$ and RuO_2.

4. Conclusions

In summary, we successfully constructed a series of $RuO_2/xCeO_2$ heterostructured catalysts by using a two-step impregnation-pyrolysis method. Comprehensive phase and electronic structure characterizations validate the formation of heterojunction interfaces and interfacial charge transfer, resulting in reduced Ru average oxidation state and diminished lattice oxygen content. The developed $RuO_2/0.5CeO_2$ catalyst delivers exceptional acidic OER performance with a low overpotential of 214 mV and excellent stability for 550 h at 10 mA cm^{-2}, outperforming commercial RuO_2. $RuO_2/0.5CeO_2$ as anode achieves a voltage of 1.59 V at 1 A cm^{-2} and operation stably for over 300 h at 500 mA cm^{-2} with a performance degradation rate of only 0.07 mV h^{-1}. ATR-SEIRAS experiments coupled with DFT calculations reveal that the heterointerface-driven AEM pathway effectively suppresses lattice oxygen oxidation while facilitating *OOH intermediate formation through the bridging of O, thereby establishing an optimal activity-stability synergy. This work proposes a heterointerface engineering strategy for designing efficient and stable Ru-based electrocatalysts toward practical hydrogen production.

Author contributions

Tenghao Liu: investigation, experiment, writing original draft. Quan Zhou: conceptualization, methodology, investigation, supervision. Liu Yang: methodology, formal analysis. Yining Zhang: investigation, supervision. Rongyue Wang: supervision, resources, project administration. Zhongwei Chen: writing – review & editing, supervision, resources, project administration, funding acquisition, formal analysis, conceptualization. All authors commented on the final manuscript.

Conflicts of interest

The authors declare that they have no known competing financial interests or personal relationships that could have appeared to influence the work reported in this paper.

Data availability

The data supporting this article have been included as part of the ESI.

Acknowledgements

This work is supported by the Strategic Priority Research Program of the Chinese Academy of Sciences, Grant No. XDB0600200, the Key Research and Development Program of

Shaanxi Province (Grant No.2024CY-GJHX-25), and State Key Laboratory of Catalysis, No 2024SKL-B-008.

Notes and references

1 S. Zhou, L. Shi, Y. Li, T. Yang and S. Zhao, *Adv. Funct. Mater.*, 2024, **34**, 1–28.

2 T. Reier, H. N. Nong, D. Teschner, R. Schlögl and P. Strasser, *Adv. Energy Mater.*, 2017, **7**, 1601275.

3 H. Wu, Y. Wang, Z. Shi, X. Wang, J. Yang, M. Xiao, J. Ge, W. Xing and C. Liu, *J. Mater. Chem. A*, 2022, **10**, 13170–13189.

4 Z. Chen, L. Guo, L. Pan, T. Yan, Z. He, Y. Li, C. Shi, Z. F. Huang, X. Zhang and J. J. Zou, *Adv. Energy Mater.*, 2022, **12**, 1–47.

5 L. An, C. Wei, M. Lu, H. Liu, Y. Chen, G. G. Scherer, A. C. Fisher, P. Xi, Z. J. Xu and C. H. Yan, *Adv. Mater.*, 2021, **33**, 1–31.

6 Y. Lin, Y. Dong, X. Wang and L. Chen, *Adv. Mater.*, 2023, **35**, 1–38.

7 S. Kaushik, X. Xiao and Q. Xu, *EnergyChem*, 2023, **5**, 100104.

8 C. Rong, K. Dastafkan, Y. Wang and C. Zhao, *Adv. Mater.*, 2023, **35**, 2211884.

9 Q. Wang, Y. Cheng, H. B. Tao, Y. Liu, X. Ma, D. S. Li, H. Bin Yang and B. Liu, *Angew. Chemie - Int. Ed.*,2023, **135**, e202216645.

10 Z. Pu, T. Liu, G. Zhang, H. Ranganathan, Z. Chen and S. Sun, *ChemSusChem*, 2021, **14**, 4636–4657.

11 M. Chatenet, B. G. Pollet, D. R. Dekel, F. Dionigi, J. Deseure, P. Millet, R. D. Braatz, M. Z. Bazant, M. Eikerling, I. Staffell, P. Balcombe, Y. Shao-Horn and H. Schäfer, *Chem. Soc. Rev.*, 2022, **51**, 4583–4762.

12 R. T. Recent advances in proton exchange membrane water electrolysisLiu, Z. L. Xu, F. M. Li, F. Y. Chen, J. Y. Yu, Y. Yan, Y. Chen and B. Y. Xia, *Chem. Soc. Rev.*, 2023, **52**, 5652–5683.

13 H. J. W. Li, Y. Lin, J. Duan, Q. Wen, Y. Liu and T. Zhai, *Chem. Soc. Rev.*, 2024,**53**, 10709-10740

14 C. Zhou, L. Li, Z. Dong, F. Lv, H. Guo, K. Wang, M. Li, Z. Qian, N. Ye, Z. Lin, M. Luo and S. Guo, *Nat. Commun.*, 2024, **15**, 9774.

15 J. Zhu, X. Sun, N. Feng, B. Zhao, M. Qiu, J. Xu and W. Luo, *J. Am. Chem. Soc.*, 2025, **147**, 47454–47466.

16 J. Bao, Y. Gu, B. Su, X. Sun, H. Zhang, K. Wang, X. Lin, C. J. Yang, B. Yang, Z. Li, C. L. Dong, Q. Zheng, M. Qiu, L. Lei, C. Yuan, Z. Shao and Y. Hou, *Angew. Chemie - Int. Ed.*, 2025, **137**, e202515362.

17 X. Wang, X. Wan, X. Qin, C. Chen, X. Qian, Y. Guo, Q. Xu, W. Bin Cai, H. Yang and K. Jiang, *ACS Catal.*, 2022, **12**, 9437–9445.

18 C. Wang, Q. Geng, L. Fan, J. X. Li, L. Ma and C. Li, *Nano Res. Energy*, 2023, **2**, e9120070–e9120070.

19 D. Chen, R. Yu, K. Yu, R. Lu, H. Zhao, J. Jiao, Y. Yao, J. Zhu, J. Wu and S. Mu, *Nat. Commun.*, 2024, **15**, 1–11.

20 K. Sun, W. Mao, L. Jin, W. Shi, W. Niu, C. Wei, Y. He, Q. Yan, R. Wang, Y. Li and B. Zhang, *Angew. Chemie - Int. Ed.*, 2025, **64**, 1–7.

21 W. Yang, Z. Wang, J. Zhang, L. Jia, J. Li, X. Chen, X. Liu, H. Zhang, J. Lin, M. Zhao and Q. Chen, *Angew. Chemie - Int. Ed.*, 2025, **137**, e202509768.

22 J. Wang, D. Wang, Y. Xiang, W. Yue, M. Sun, J. Sun and J. Li, *Nano Energy*, 2025, **145**, 111452.

23 G. Wang, W. Wan, M. Chen, J. Li, X. Wu, S. Huang, K. Li, X. Tian and Z. Kang, *Int. J. Hydrogen Energy*, 2024, **71**, 804–810.

24 Y. Zhang, S. Zhang, Y. Yue, M. Xiao, G. Cheng, Y. Pan, S. Liu, C. Li, J. Zhao and X. Li, *ACS Catal.*, 2025, **15**, 17445–17455.

25 K. Zhang and R. Zou, *Small*, 2021, **17**, 1–40.

26 H. Liu, Y. Zhang, Z. Liu, S. Wang, X. Mu, Q. Zhang, W. Cao, S. Liu, D. Wang and Z. Dai, *J. Am. Chem. Soc.*, 2025, **147**, 44141–44151.

27 F. Zhou, L. Zhang, J. Li, Q. Wang, Y. Chen, H. Chen, G. Lu, G. Chen, H. Jin, S. Wang and J. Wang, *Eng. Reports*, 2021, **3**, 1–22.

28 X. Cao, L. Miao, W. Jia, H. Qin, G. Lin, R. Ma, T. Jin and L. Jiao, *Nat. Commun.* , 2025, **16**, 1–11.

29 Y. Hao, S. F. Hung, C. Tian, L. Wang, Y. Y. Chen, S. Zhao, K. S. Peng, C. Zhang, Y. Zhang, C. H. Kuo, H. Y. Chen and S. Peng, *Angew. Chemie - Int. Ed.*, 2024, **63**, e202402018.

30 S. S. Kumar and H. Lim, *Sustain. Energy \& Fuels*, 2023, **7**, 3560–3583.

31 L. Deng, S. Liu, D. Liu, Y. M. Chang, L. Li, C. Li, Y. Sun, F. Hu, H. Y. Chen, H. Pan and S. Peng, *Small*, 2023, **19**, 1–10.

32 M. Wu, Y. Fan, Y. Huang, D. Wang, Y. Xie, A. Wu and C. Tian, *Nano Res.*, 2024, **17**, 6931–6939.

33 J. Huang, H. Sheng, R. D. Ross, J. Han, X. Wang, B. Song and S. Jin, *Nat. Commun.*, 2021, **12**, 3036.

34 J. Liu, T. Wang, X. Liu, H. Shi, S. Li, L. Xie, Z. Cai, J. Han, Y. Huang, G. Wang and Q. Li, *ACS Catal.*, 2023, **13**, 5194–5204.

35 Z. Dong, C. Zhou, W. Chen, F. Lin, H. Luo, Z. Sun, Q. Huang, R. Zeng, Y. Tan, Z. Xiao, H. Huang, K. Wang, M. Luo, F. Lv and S. Guo, *Adv. Funct. Mater.*, 2024, **2400809**, 1–8.

36 H. Zhao, J. Yin and P. Xi, *Trans. Tianjin Univ.*, 2023, **29**, 395–405.

37 Z. Guan, Q. Chen, L. Liu, C. Xia, L. Cao and B. Dong, *Nanoscale*, 2024, **16**, 10325–10332.

38 Y. Wu, R. Yao, K. Zhang, Q. Zhao, J. Li and G. Liu, *Chem. Eng. J.*, 2024, **479**, 147939.

39 S. Chen, H. Huang, P. Jiang, K. Yang, J. Diao, S. Gong, S. Liu, M. Huang, H. Wang and Q. Chen, *ACS Catal.*, 2020, **10**, 1152–1160.

40 X. Song, H. Zheng, J. Zhang, X. Zhang, J. Cui, M. Ayyob, C. Liu, P. Su and Z. Chen, *ACS Catal.*, 2025, **15**, 11366–11376.

41 L. Wang, S. F. Hung, S. Zhao, Y. Wang, S. Bi, S. Li, J. J. Ma, C. Zhang, Y. Zhang, L. Li, T. Y. Chen, H. Y. Chen, F. Hu, Y. Wu and S. Peng, *Nat. Commun.*, 2025, **16**, 3502.

42 W. Xia, K. Yuan, X. Cao, H. Qin, G. Lin, J. Zhang, T. Jin, Q. Wang and L. Jiao, *ACS Catal.*, 2025, **15**, 768–779.

43 W. Gou, Z. Xia, X. Tan, Q. Xue, F. Ye, S. Dai, M. Zhang, R. Si, Y. Zou, Y. Ma, J. C. Ho and Y. Qu, *Nano Energy*, 2022, **104**, 107960.

View Article Online
DOI: 10.1039/D6TA01093H

44 M. Qi, X. Du, X. Shi, S. Wang, B. Lu, J. Chen, S. Mao, H. Zhang and Y. Wang, *J. Am. Chem. Soc.*, 2025, **147**, 18295–18306.

45 H. Wu, Z. Fu, J. Chang, Z. Hu, J. Li, S. Wang, J. Yu, X. Yong, G. I. N. Waterhouse, Z. Tang, J. Chang and S. Lu, *Nat. Commun.*, 2025, **16**, 1–12.

46 Y. Yu, G. Huang, W. Fan, Z. Fan, H. Gao, D. Wu, T. Wang, J. Li, X. Shi, Z. Kang, P. Deng, Y. Liang, X. Tian and P. Rao, *Adv. Funct. Mater.*, 2025, **23636**, 1–10.

Footnotes

Electronic supplementary information (ESI) available: Fig. S1–S12, including SEM images, LSV and CV curves, EIS analysis, and computation models; Tables S1–S5.

View Article Online
DOI: 10.1039/D6TA01093H

The data that support the findings of this study are available in the electronic supplementary information of this article. Electronic supplementary information (ESI) available: Fig. S1–S12, including SEM images, LSV and CV curves, EIS analysis, and computation models; Tables S1–S5.